NANO LETTERS
2007
Vol. 7, No. 9
2920−2925

Iron Phosphide Nanostructures Produced from a Single-Source Organometallic Precursor: Nanorods, Bundles, Crosses, and Spherulites

Anna T. Kelly,[†] Irene Rusakova,[‡] Teyeb Ould-Ely,[†] Cristina Hofmann,[†] Andreas Lüttge,[§] and Kenton H. Whitmire*,[†]

Department of Chemistry, MS 60, and Department of Earth Science, MS 126, Rice University, 6100 Main Street, Houston, Texas 77005-1892, and Texas Center for Superconductivity, University of Houston, Houston, Texas 77204-5931

Received June 4, 2007; Revised Manuscript Received July 26, 2007

ABSTRACT

Single-source molecular precursors were found to produce iron phosphide materials. In a surfactant system of trioctylamine and oleic acid, $H_2Fe_3(CO)_9P^tBu$ reacted to form $Fe_4(CO)_{12}(P^tBu)_2$, which decomposed to give Fe_2P nanorods and "bundles." Control of the morphology obtained was possible by varying the surfactant system; addition of increasing amounts of oleic acid resulted in crystal splitting, while the addition of microliter amounts of an alkane enhanced the crystal splitting to give sheaflike structures. The different morphologies seen were attributed to imperfect crystal growth mechanisms.

The synthesis of one-dimensional nanostructures is a rapidly expanding area of interest.[1] There is a great deal still to be learned regarding the growth mechanisms involved in these systems that can provide control over the size and shape of the materials. The morphology of nanomaterials is known to influence the physical properties observed (i.e., magnetic, optical, electronic, etc.). An ideal method for synthesizing nanomaterials would also allow for the formation of a pure, single-phase material.

Transition metal phosphides are an interesting class of materials exhibiting magnetic, catalytic, magnetoresistant, and magnetocaloric properties.[2−5] Iron phosphides exist in a variety of phases, including FeP, Fe_2P, and Fe_3P. Both Fe_3P and Fe_2P are ferromagnetic, with Curie temperatures (T_c) of 716 and 217 K, respectively.[6,7] While there has been an interest in the magnetic properties of metal phosphides for decades, there has not been much exploration of these materials on the nanoscale. Traditionally, bulk iron phosphide materials have been synthesized by combining iron and phosphorus and heating to high temperatures.[8,9] The problem with such synthetic methods is the parallel formation of a variety of phases that are often difficult to separate. The relatively high temperatures at which these reactions are carried out also prohibit the formation of thin films and nanostructures.

A variety of methods for producing nanoscale iron phosphides have been reported. The reduction of iron phosphate nanoparticles in a H_2/Ar atmosphere resulted in the formation of a mixture of FeP and Fe_2P nanoparticles.[2,10] The phase produced was dependent upon the temperature to which the particles were heated; the FeP phase was evident at 700 °C and Fe_2P was present at 1100 °C. Another more common approach is the use of separate sources of iron and phosphorus. Iron phosphide (FeP) nanowires and nanorods synthesized by the injection of a solution of iron pentacarbonyl in trioctylphosphane (TOP) into a mixture of trioctylphosphine oxide (TOPO) and TOP, where TOP served as the phosphorus source.[11] Similar methods have been reported in which some variant of an iron carbonyl was used as the iron source.[11−13] Although these methods have produced pure phases of iron phosphide nanomaterials, there was no control over which phase was obtained.

In contrast, the use of single-source molecular precursors will presumably offer a method in which the desired phase can be targeted. Single-source molecular precursors may allow for the control of as well as isolation of pure products.[14] Only one previous attempt to synthesize iron phosphide nanomaterials via a single source molecular precursor has been reported; the decomposition of $Fe(CO)_4[PPh_2CH_2CH_2$-

---

* Corresponding author. E-mail: whitmir@rice.edu.
[†] Department of Chemistry, Rice University.
[‡] Texas Center for Superconductivity, University of Houston.
[§] Department of Earth Science, Rice University.

10.1021/nl0713225 CCC: $37.00

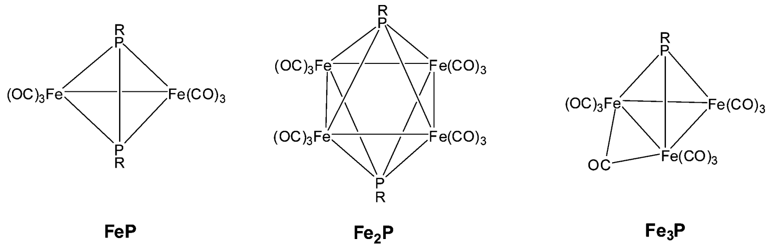

Figure 1. Iron phosphorus clusters.

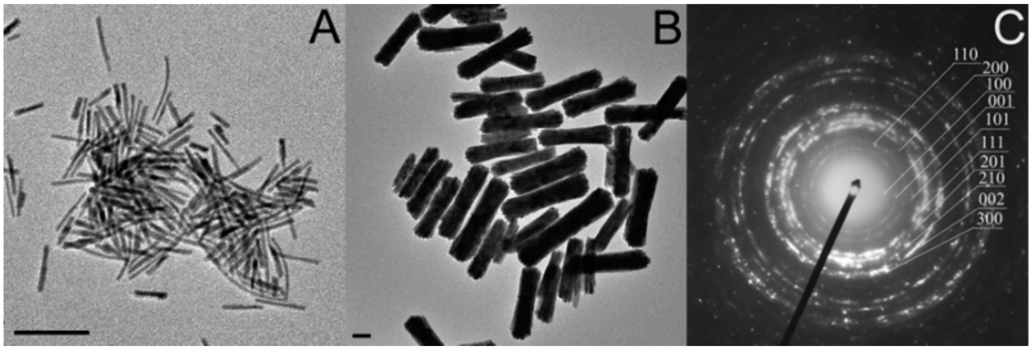

Figure 2. Transmission electron microscopy (TEM) images of iron phosphide nanorods synthesized from 0.5 mmol precursor in different solvent ratios: (A) 7:1 TOA:OA, aspect ratio 11; (B) 6:2 TOA:OA, aspect ratio 5; (C) SAED pattern of iron phosphide nanorods. All scale bars represent 100 nm.

$Si(OMe)_3$] in a silica xerogel matrix resulted in the formation of Fe_2P nanoclusters.[15]

We have investigated the use of iron−phosphorus carbonyl clusters as single-source precursors to iron phosphide materials. There are a variety of such clusters that have been synthesized with different stoichiometric ratios of iron to phosphorus (Figure 1). We hypothesized that cluster complexes would function better than the simpler complexes as single-source precursors because of the greater number of phosphorus−metal interactions which more closely mimic that found in the solid-state materials. Indeed, metal clusters can be viewed as fragments of metal and metallic alloy lattices. Furthermore, in the clusters, the Fe−P bonds are usually covalent, whereas in the substituted complexes, dative bonds are more common; therefore, the loss of the phosphorus fragment is more likely to occur during the decomposition of the simpler complexes, resulting in the synthesis of phosphorus-poor products. The synthetic strategy involves the reaction of iron carbonyls and alkyl phosphines (RPH_2) or alkyl phosphine halides (RPX_2).[16−18] The decomposition of such clusters should provide an efficient means of synthesizing transition metal phosphides having the same stoichiometry as the parent cluster.

The cluster $H_2Fe_3(CO)_9P^tBu$ was examined as a single-source precursor targeted to the Fe_3P phase. The formation of iron phosphide nanoparticles was accomplished by the decomposition of the cluster in the presence of a surfactant system of trioctylamine (TOA) and oleic acid (OA). Surprisingly X-ray powder diffraction (XRPD) analysis of the product indicated formation of the Fe_2P phase (Supporting Information Figure S1), as did elemental analysis. Observed (calculated) for Fe_2P: Fe 71.7 (78.3), P 20.1 (21.7); Galbraith Analytical Laboratories. Upon investigation of the decomposition mechanism, however, it was discovered that the precursor transformed in the solvent system before decomposition to the iron phosphide material took place. The precursor is highly acidic,[19] and in the presence of TOA, it was first deprotonated as evidenced by Fourier transform infrared (FT-IR) spectroscopy. Further thermal rearrangement of the cluster after deprotonation resulted in the formation of $Fe_4(CO)_{12}(P^tBu)_2$ (Supporting Information Table S1 and Figure S2). The observed transformations are displayed in eq 1.

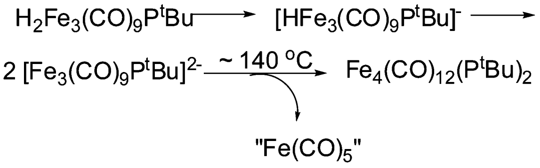

$$H_2Fe_3(CO)_9P^tBu \longrightarrow [HFe_3(CO)_9P^tBu]^- \longrightarrow$$
$$2\,[Fe_3(CO)_9P^tBu]^{2-} \underset{\text{"}Fe(CO)_5\text{"}}{\xrightarrow{\sim 140\ ^{o}C}} Fe_4(CO)_{12}(P^tBu)_2 \qquad (1)$$

By varyiation of the concentrations of TOA and OA, different nanoparticle shapes were observed (Figure 2). Using a ratio of TOA:OA 7:1 (v:v), individual iron phosphide rods having an aspect ratio of ∼11 were obtained (Figure 2A). When the concentration of OA was increased (TOA:OA = 6:2 or 4:4), a more complex system of split nanocrystals was obtained (Figure 2B depicts those synthesized from 6:2 ratio). Both the 6:2 and 4:4 TOA:OA surfactant systems produced similar bundles, but the 4:4 system resulted in a more monodisperse product. The bundles had an average size of 415 ± 28 nm × 70 ± 9 nm and an average aspect ratio of 6, whereas the bundles synthesized in the 6:2 solvent system had an average size of 403 ± 65 nm × 90 ± 17 nm and an average aspect ratio of 5.

The polycrystalline selected area electron diffraction (SAED) pattern (Figure 2C) recorded from the bundles

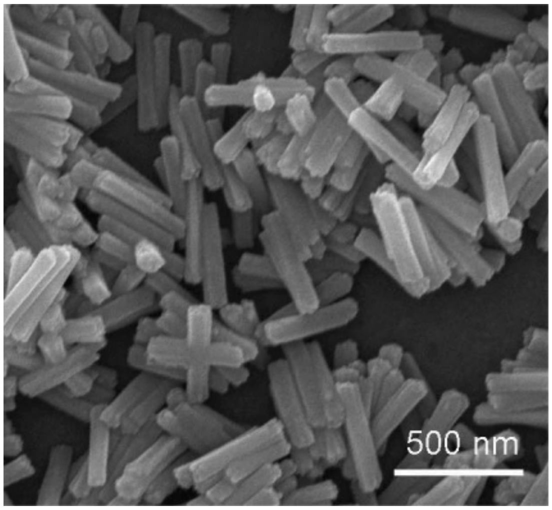

Figure 3. SEM image of bundles of Fe_2P nanorods synthesized from a 4:4 TOA:OA surfactant system.

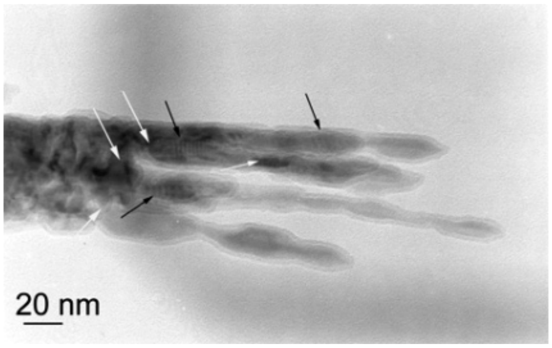

Figure 4. A split rod. Black arrows indicate moiré fringes, while white arrows indicate the location of splitting.

confirmed that the material is single-phase Fe_2P (hexagonal, $P\bar{6}2m$, $a = 5.877$ Å, $c = 3.437$ Å, Figure S3). Single-crystal SAED patterns and high-resolution transmission electron microscopy (HR-TEM) images indicated growth of the rods along the *c*-axis. Electron diffraction spectroscopy confirmed that all bundles are composed of iron and phosphorus; no other elements were observed. Scanning electron microscopy (SEM) analysis provided a three-dimensional view of the bundles (Figure 3).

Upon increase of the oleic acid concentration, the rods acquire a bundle-like morphology. Initially from the TEM images, the rods appeared to be closely packed assemblies; however, upon further examination, it was found that splitting was occurring along the *c*-axis (Figure 4). Similar growth initiated by crystal splitting has been recently observed by our group for lead sulfide (PbS) nanorods as well as by Tang and Alivisatos in the Bi_2S_3 system.[20,21] Unlike the Bi_2S_3 system, the crystal structure of Fe_2P (Figure S8) possesses neither one-dimensional chain structures nor two-dimensional layers in the direction of growth that would provide obvious splitting vectors for the growing crystal. The asymmetry of this space group, however, promotes fast growth of the *C* face, and a high density of crystal defects was observed in proximity to the splitting. It is possible that these defects arise from metal atom misplacement during fast growth as the Fe atoms in this structure can form either tetrahedral or square pyramidal configurations, but this hypothesis will require further study to confirm. Unfortunately the nature of the splitting makes it difficult to obtain high-quality HR-TEM micrographs at the splitting junctions. Overlapping of individual rods also complicates obtaining high-quality HR-TEM images. Rotational moiré fringes are observed in the TEM images as a result of small angular deviation and overlapping of individual rods after splitting.

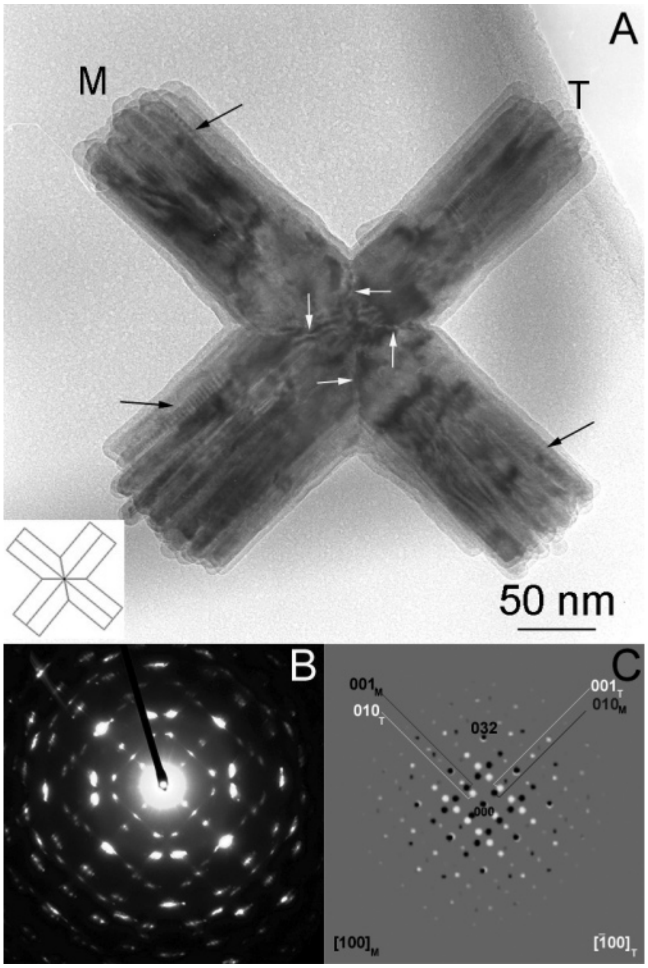

Figure 5. (A) BF TEM image of bundle showing a cross-shaped morphology: black arrows indicate moiré fringes while white arrows indicate the twin boundaries; M, matrix bundle; T, twin bundle; inset, schematic figure of a penetration twin. (B, C) Experimental and simulated SAED patterns of cross-shaped bundle. Black reflections in (C) arise from the matrix bundle of rods, and white reflections arise from the twin bundle of rods.

While the simple bundles dominated in all of the variations studied, cross-shaped and T-shaped bundles were also observed (Figure S4). From the initial TEM and SEM images showing cross-shaped nanoparticles, it was unclear whether they arose from random overlap of the rod-shaped crystals or from an interrupted growth process. In order to shed light on the growth mechanism, we investigated their microstructure using TEM diffraction coupled with bright field (BF) and dark field (DF) imaging. It is clear from the BF image of one of the cross-shaped bundles (Figure 5A) that the structure had grown from the same seed crystal and formed

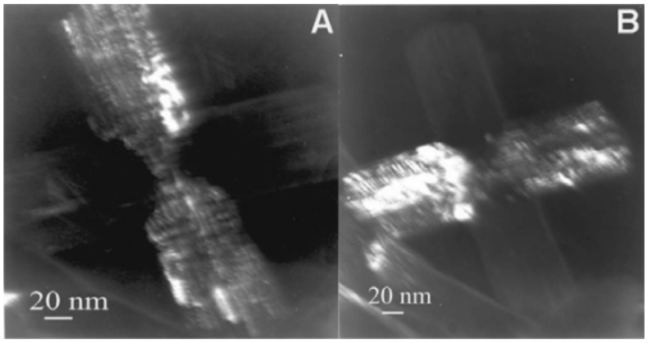

Figure 6. Central DF TEM images of a cross-shaped bundle using reflections from matrix (A) and twin (B).

as the result of a twinning mechanism leading to so-called penetration twins.

The X-shaped junction seen using TEM studies is indeed similar to features observed in penetration twins typical for various minerals, including staurolite (for schematic representation, see Figure 5A inset).[22] The formation of growth twins results from an interruption in the crystal lattice during growth. When crystals join to form a twin during nucleation, they should develop to become equal in size, which is observed in this system. In support of this intergrowth mechanism is the observation that the crosses are only observed with arms at ~90° angles, which supports the contention that the arm orientation is controlled by crystallographic twinning.

Further support of this mechanism is provided by the SAED pattern, which is consistent with twinning of the crystal. The matrix bundle has a [100] zone axis orientation whereas the twin bundle has a [$\bar{1}$00] zone axis orientation. The twinning plane is (032) and the twinning law is a 4-fold rotation (tetrad) around [100]. Splitting and azimuthal deviations of reflections in Figure 5B are caused by small-angle deviations of individual rods inside a bundle. The rotational moiré fringes that we observed in BF TEM images originate from such deviations as well as from overlapping of individual rods inside a bundle. The thickness fringes observed result from overlapping of the split crystals. The DF TEM images (Figure 6) further confirm the twinning mechanism of the growth of the cross-shaped bundles; the X-shaped junction is also observed in these images. HR TEM images reveal the presence of other planar defects (stacking faults) in the microstructure of bundles, which contribute to splitting of the rods (Figure 7). The presence of stacking faults explains the observation of streaks in the SAED pattern (Figure 5B).

Additional changes in the morphologies obtained were seen upon addition of controlled amounts of alkanes to the decomposition. When alkanes, such as hexane, nonane, and tridecane were added, an even more complex crystal splitting was observed, having a haystack (Figure 8A), dumbbell (Figure 8B), or spherulitic morphology (Figure 8C). The identity of the alkane was not found to be important. Both TEM and SEM images were obtained (Figure 8 and Figure S5). As was seen for the bundles discussed previously, cross-shaped and T-shaped bundles (Figures S6 and S7) were also seen in these experiments.

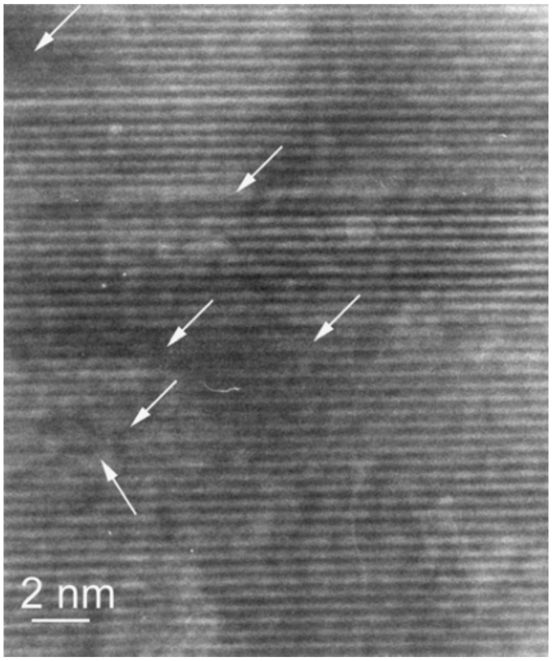

Figure 7. HR TEM image recorded from the area close to the center of the bundle showing planar defects (stacking faults) as marked by white arrows.

All decompositions produced Fe_2P nanorods. It has been well documented that the surfactants employed in the synthesis of nanoparticles influence the shape and size of the resulting nanomaterials.[23] Others have also reported the synthesis of metal phosphide nanorods.[11−13,24] In one of those systems, tri-*n*-octylphosphine and oleylamine were used as surfactants. The formation of nanorods was explained by the cooperative effect of the surfactants along with the intrinsically anisotropic crystal structure of the phosphides.[24] As mentioned previously, Fe_2P has a hexagonal crystal structure ($P\bar{6}2m$ space group, Figure S8), which is known for anisotropic growth. The structure has a unique [001] axis, and growth occurs along this direction. Crystal splitting in the Fe_2P system appears to occur from the high concentration of defects produced due to the high rate of growth in the *c* direction. While similar structures have been shown to arise from crystal splitting in Bi_2S_3,[21] for Fe_2P one-dimensional or layer-like arrangements of the atoms that would give rise to cleavage planes are not obvious in Fe_2P in any crystallographic direction.

As far as the effect of surfactants on the growth and splitting, we found that increasing the concentration of oleic acid appears to cause the rods to split. From the system in which trioctylamine and oleic acid are in a 7:1 ratio, single iron phosphide nanorods are synthesized. However, upon increase of the concentration of oleic acid, splitting of the rods occurs. Additionally, when alkanes were added in microliter amounts to the reaction, a more complex dumbbell-shaped splitting was observed.

For the Tang and Alivisatos[21] synthesis of Bi_2S_3, the various nanostructures were synthesized by the reaction of elemental sulfur and a bismuth carboxylate in 1-octadecene. The control of shape in that system was achieved via variations in the injection temperature of sulfur. In contrast,

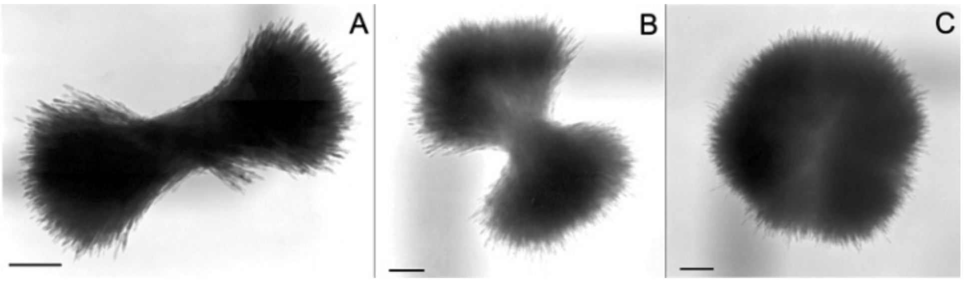

Figure 8. Effect of addition of alkanes. All scale bars represent 200 nm.

for Fe_2P, the temperature was not varied; instead, addition of small amounts of alkanes caused the formation of the dumbbell-shaped bundles. A new surface area forms every time the crystal splits, and the introduction of molecules that would stabilize the growing surfaces would favor crystal splitting. Increasing the amount of oleic acid, a good stabilizing surfactant, also appeared to promote crystal splitting. Sunagawa reported that split growth is seen often in systems having high growth rates.[22] Nucleation and growth occur rapidly in the iron phosphide system, as can be seen in a TEM image taken from a 1-min reaction (reaction time after the solution turned black, Figure S9).

Many of the shapes seen in our synthesis as well as in the recently reported work with bismuth sulfide resemble those seen in spherulites and other forms of minerals, which are also believed to form via a crystal splitting growth mechanism.[22] While the precise formation mechanism of spherulites via crystal splitting is not well understood, there has been speculation regarding the possible causes.[25−27] There are two classes of spherulites formed by two distinctly different overall growth processes. In the first, growth occurs radially from a common nucleation site. The second growth process begins with a single fiber that branches as growth continues, forming a sheaf and eventually evolving into the spherulite. On the basis of these classifications, it appears as though the iron phosphide system follows a similar growth process as that leading to the second class of spherulites. The evolution from rod-shaped and split crystals to dumbbell-shaped bundles and spherulites occurred with the incremental addition of microliter amounts of alkanes to the system before decomposition of the precursor. Keith and Padden[25] reported the presence of low molecular weight components, which may be considered impurities, to be common in spherulite-forming solutions. The presence of the alkanes in small concentrations seems to have a significant impact on the growth kinetics. We may speculate that the alkanes interrupted the crystallization process, leading to a bifurcation of the growth process and consequently enhancing the splitting of the rods.

Information regarding the temperature-dependent magnetic behavior of the nanorods as the temperature was varied is seen in the zero-field-cooling (ZFC) and field-cooling (FC) graphs. Figure 9 presents the ZFC/FC of three of the different iron phosphide morphologies synthesized. Interestingly, the blocking temperature (T_B) was seen to increase from a T_B centered around 124 K for well dispersed nanorods (Figure 9A) to a T_B of 180 K for rods that had a bundle-like morphology (simple splitting, Figure 9B), although there was a broader distribution of blocking temperatures, probably due to the distribution of the magnetic size as a result of the dipolar coupling within the rods. A further increase in T_B was observed in the more complex dumbbell-shaped system (Figure 9C) where the blocking temperature reaches 205 K. This increase in blocking temperature with increased interparticle interaction was not unexpected, as it has been reported that with increasing strength of dipolar interactions, the mean T_B value increases.[28−30]

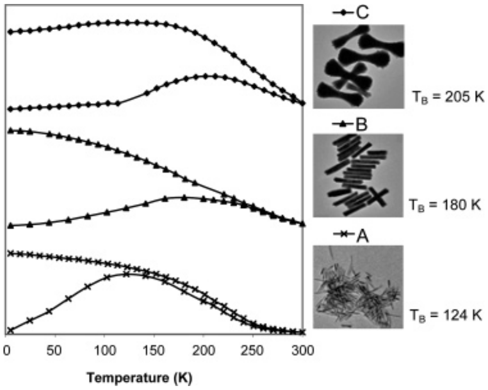

Figure 9. ZFC/FC graph of iron phosphide nanorods at 1000 Oe.

The hysteresis loops indicate the presence of a coercive field at 5 K (Supporting Information, Figure S10). A very small hysteresis remains at 250 K, above the Curie temperature. This suggests that a small amount of impurity is most likely present in the product. In the decomposition mechanism proposed in eq 1, $Fe(CO)_5$ is produced as a byproduct. The thermal decomposition of $Fe(CO)_5$ has been reported to produce both iron and iron oxide nanoparticles.[31−35] The presence of these nanoparticles would explain the observed magnetic properties. The magnetic moment calculated from the saturation magnetization (M_s) at 5 K was 2.28 μ_B, which is similar in magnitude to the most recently reported magnetic moment of single-crystalline Fe_2P (2.81 μ_B; determined by neutron diffraction).[8] It is important to note that the magnetic measurements on Fe_2P have been found to be very sensitive to impurities and deviations from an ideal stoichiometry. Values reported for the magnetic moment, using a variety of methods for determination as well as a variety of temperatures, have ranged from 2 to 3 μ_B.[6,36−38] Another reason proposed for the wide range of reported magnetic moments has to do with the large magnetic anisotropy of Fe_2P, resulting in a slow approach to saturation in measurements made using polycrystalline samples.[39]

In conclusion, we have successfully used a soluble single-source molecular precursor to synthesize iron phosphide nanomaterials. A variety of different morphologies, due to crystal splitting, were seen as a result of changing synthetic parameters (i.e., ratio of oleic acid to trioctylamine and addition of small amounts of alkanes). Additional cross-shaped structures were also observed and attributed to the twinning of two individual bundles during growth as the result of an interrupted growth process. Current work aims at synthesizing other Fe_xP_y phases, especially the ferromagnetic Fe_3P that has a higher T_c, and establishing more definitively the relationship between precursor stoichiometry and final product.

Acknowledgment. We thank Rice University, the Robert A. Welch Foundation (C-0976), and the National Science Foundation (CHE-0719396) for funding.

Supporting Information Available: Materials, characterization, and synthetic procedures for the different morphologies synthesized, XRPD image, FT-IR data in support of the proposed decomposition mechanism, SAED information, Fe_2P crystal structure information, and additional TEM and SEM images. This information is available free of charge via the Internet at http://pubs.acs.org.

References

(1) Xia, Y.; Yang, P.; Sun, Y.; Wu, Y.; Mayers, B.; Gates, B.; Yin, Y.; Kim, F.; Yan, H. *Adv. Mater.* **2003**, *15*, 353−389.
(2) Brock, S. L.; Perera, S. C.; Stamm, K. L. *Chem.-Eur. J.* **2004**, *10*, 3364−3371.
(3) Stinner, C.; Prins, R.; Weber, T. *J. Catal.* **2001**, *202*, 187−194.
(4) Luo, F.; Su, H.-L.; Song, W.; Wang, Z.-M.; Yan, Z.-G.; Yan, C.-H. *J. Mater. Chem.* **2004**, *14*, 111−115.
(5) Fruchart, D.; Allab, F.; Balli, M.; Gignoux, D.; Hlil, E. K.; Koumina, A.; Skryabina, N.; Tobola, J.; Wolfers, P.; Zach, R. *Physica A* **2005**, *358*, 123−135.
(6) Meyer, A. J. P.; Cadeville, M. C. *J. Phys. Soc. Jpn.* **1962**, *17* (*Suppl. B-I*), 223−225.
(7) Fujii, H.; Uwatoko, Y.; Motoya, K.; Ito, Y.; Okamoto, T. *J. Phys. Soc. Jpn.* **1988**, *57*, 2143−2153.
(8) Koumina, A.; Bacmann, M.; Fruchart, D.; Soubeyroux, J.-L.; Wolfers, P.; Tobola, J.; Kaprzyk, S.; Niziol, S.; Mesnaoui, M.; Zach, R. *Ann. Chim.*−*Sci. Mater.* **1998**, *23*, 177−180.
(9) Bailey, R. E.; Duncan, J. F. *Inorg. Chem.* **1967**, *6*, 1444−1447.
(10) Stamm, K. L.; Garno, J. C.; Liu, G.-y.; Brock, S. L. *J. Am. Chem. Soc.* **2003**, *125*, 4038−4039.
(11) Qian, C.; Kim, F.; Ma, L.; Tsui, F.; Yang, P.; Liu, J. *J. Am. Chem. Soc.* **2004**, *126*, 1195−1198.
(12) Chen, J.-H.; Tai, M.-F.; Chi, K.-M. *J. Mater. Chem.* **2004**, *14*, 296−298.
(13) Park, J.; Koo, B.; Hwang, Y.; Bae, C.; An, K.; Park, J.-G.; Park, H. M.; Hyeon, T. *Angew. Chem., Int. Ed.* **2004**, *43*, 2282−2285.
(14) Veith, M. *J. Chem. Soc., Dalton Trans.* **2002**, 2405−2412.
(15) Carpenter, J. P.; Lukehart, C. M.; Milne, S. B.; Stock, S. R.; Wittig, J. E.; Jones, B. D.; Glosser, R.; Zhu, J. G. *J. Organomet. Chem.* **1998**, *557*, 121−130.
(16) Huttner, G.; Schneider, J.; Mohr, G.; Von Seyerl, J. *J. Organomet. Chem.* **1980**, *191*, 161−169.
(17) Lang, H.; Zsolnai, L.; Huttner, G. *J. Organomet. Chem.* **1985**, *282*, 23−51.
(18) Vahrenkamp, H.; Wucherer, E. J.; Wolters, D. *Chem. Ber.* **1983**, *116*, 1219−1239.
(19) Deck, W.; Schwarz, M.; Vahrenkamp, H. *Chem. Ber.* **1987**, *120*, 1515−1521.
(20) Ould-Ely, T.; Mandal, T.; Rusakova, I.; Asokan, S.; Wong, M. S.; Whitmire, K. H. Manuscript in preparation.
(21) Tang, J.; Alivisatos, A. P. *Nano Lett.* **2006**, *6*, 2701−2706.
(22) Sunagawa, I. *Crystals: Growth, Morphology, and Perfection*; Cambridge University Press: Cambridge, U.K., 2005.
(23) Jun, Y.-w.; Choi, J.-s.; Cheon, J. *Angew. Chem., Int. Ed.* **2006**, *45*, 3414−3439.
(24) Park, J.; Koo, B.; Yoon, K. Y.; Hwang, Y.; Kang, M.; Park, J.-G.; Hyeon, T. *J. Am. Chem. Soc.* **2005**, *127*, 8433−8440.
(25) Keith, H. D.; Padden, F. J. *J. Appl. Phys.* **1963**, *34*, 2409−2421.
(26) Keller, A.; Waring, J. R. S. *J. Polym. Sci.* **1955**, *17*, 447−472.
(27) Granasy, L.; Pusztai, T.; Borzsonyi, T.; Toth, G.; Tegze, G.; Warren, J. A.; Douglas, J. F. *J. Mater. Res.* **2006**, *21*, 309−319.
(28) Nunes, W. C.; Cebollada, F.; Knobel, M.; Zanchet, D. *J. Appl. Phys.* **2006**, *99*, 08N705.
(29) Zysler, R. D.; Ramos, C. A.; De Biasi, E.; Romero, H.; Ortega, A.; Fiorani, D. *J. Magn. Magn. Mater.* **2000**, *221*, 37−44.
(30) Dormann, J. L.; Fiorani, D.; Tronc, E. *J. Magn. Magn. Mater.* **1999**, *202*, 251−267.
(31) Hyeon, T.; Lee, S. S.; Park, J.; Chung, Y.; Na, H. B. *J. Am. Chem. Soc.* **2001**, *123*, 12798−12801.
(32) Park, S.-J.; Kim, S.; Lee, S.; Khim, Z. G.; Char, K.; Hyeon, T. *J. Am. Chem. Soc.* **2000**, *122*, 8581−8582.
(33) Peng, S.; Wang, C.; Xie, J.; Sun, S. *J. Am. Chem. Soc.* **2006**, *128*, 10676−10677.
(34) Yang, J. B.; Xu, H.; You, S. X.; Zhou, X. D.; Wang, C. S.; Yelon, W. B.; James, W. J. *J. Appl. Phys.* **2006**, *99*, 08Q507/501−508Q507/503.
(35) Zhang, G. Q.; Wu, H. P.; Ge, M. Y.; Jiang, Q. K.; Chen, L. Y.; Yao, J. M. *Mater. Lett.* **2007**, *61*, 2204−2207.
(36) Lundgren, L.; Tarmohamed, G.; Beckman, O.; Carlsson, B.; Rundqvist, S. *Phys. Scr.* **1978**, *17*, 39−48.
(37) Fruchart, R.; Roger, A.; Senateur, J. P. *J. Appl. Phys.* **1969**, *40*, 1250−1257.
(38) Bellavance, D.; Mikkelsen, J.; Wold, A. *J. Solid State Chem.* **1970**, *2*, 285−290.
(39) Chandra, R.; Bjarman, S.; Ericsson, T.; Haeggstroem, L.; Wilkinson, C.; Waeppling, R.; Andersson, Y.; Rundqvist, S. *J. Solid State Chem.* **1980**, *34*, 389−396.

NL0713225